Energy Landscapes on Polymerized Liquid Crystal Interfaces

SCHOLARONE™
Manuscripts

Energy Landscapes on Polymerized Liquid Crystal Interfaces

Rachel S. Hendley,[†] *Eugenie Jumai'an,*[†] *and Michael A. Bevan**

Chemical & Biomolecular Engineering, Johns Hopkins University, Baltimore, MD 21218, USA

Hector. A. Fuster,[†] *Nicholas L. Abbott**

Chemical & Biomolecular Engineering, Cornell University, Ithaca, NY 14853, USA

Abstract

We measure and model monolayers of concentrated diffusing colloidal probes interacting with polymerized liquid crystal (PLC) planar surfaces. At topological defects in local nematic director profiles at PLC surfaces, we observe time-averaged two-dimensional particle density profiles of diffusing colloidal probes that closely correlate with spatial variations in PLC optical properties. An inverse Monte Carlo analysis of particle concentration profiles yields two-dimensional PLC interfacial energy landscapes on the kT-scale, which is the inherent scale of many interfacial phenomena (*e.g.*, self-assembly, adsorption, diffusion). Energy landscapes are modelled as the superposition of macromolecular repulsion and van der Waals attraction based on an anisotropic dielectric function obtained from the liquid crystal birefringence. Modelled van der Waals landscapes capture most net energy landscape variations and correlate well with experimental PLC director profiles around defects. Some energy landscape variations near PLC defects indicate either additional local repulsive potentials or possibly the need for more rigorous van der Waals models with complete spectral data. These findings demonstrate direct, sensitive measurements of kT-scale van der Waals energy landscapes at PLC interfacial defects and suggest the ability to design interfacial anisotropic materials and van der Waals energy landscapes for colloidal assembly.

Key words: colloidal interactions | van der Waals | anisotropic dielectric functions | diffusing colloidal probes | inverse Monte Carlo | topological defects

Introduction

Local interactions between colloids and surfaces can be used to pattern colloidal deposition and assembly of hierarchically structured materials,[1] including mimics of natural multi-functional surfaces.[2] Examples of the use of local colloid-surface interactions to mediate colloidal assembly include physical features,[3-5] electrostatics,[6-7] fields,[8-12] depletion,[13-14] and optical interactions.[15] Although van der Waals attraction is ubiquitous, and can be spatially modulated via local materials properties (*e.g.*, gold patterns[16]), there has been little exploration of patterned van der Waals interactions to mediate interfacial colloidal assembly. Practically, spatially controlling local surface dielectric functions[17] has perhaps been difficult to achieve by patterning non-uniform materials. Limited precedent for tuning van der Waals interactions in colloidal assembly processes include tuning a phase separating medium over a chemical pattern[18] and patterning particles to modify their pair interactions.[19] Understanding how spatially varying dielectric functions mediate local van der Waals interactions can provide a basis to design, control, and optimize interfacial processes (*e.g.*, adsorption, deposition, self-assembly, diffusion) in a variety of interfacial systems

---

†These authors contributed equally to this work.

*To whom correspondence should be addressed: mabevan@jhu.edu, nla34@cornell.edu

(*e.g.*, colloids, macromolecules, surfactants). In addition, understanding van der Waals interactions on the order of thermal energy, *kT*, is essential to self-assembly; *kT*-scale fluctuations are the basis for Brownian motion that enables self-assembly, and *kT*-scale attraction is the origin of condensed liquid, liquid crystalline, and crystalline states.

Recently, it has been suggested that spatially varying director profiles near surface defects of polymeric liquid crystal (PLC) microparticles can mediate an interfacial van der Waals energy landscape.[20] This prior study reported enhanced irreversible colloidal adsorption on surfaces of ~20 micron PLC microparticles in regions where liquid crystal (LC) orientation was predominantly parallel to the interface. This observation was consistent for different interfacial LC director profiles possessing topological defects. Enhanced deposition on interfacial regions with parallel LC orientations was considered to arise from an anisotropic dielectric function associated with LC birefringence. Specifically, the greater refractive index and dielectric constant associated with the parallel LC orientations correlated with higher colloidal adsorption and apparently stronger van der Waals attraction, while the lower refractive index and dielectric constant associated with the perpendicular LC orientation produced less colloidal deposition and weaker local van der Waals. In this previous study, deposition probability, as a kinetically controlled phenomena, was an indirect measure of van der Waals, suggesting the role of LC orientation and dielectric function in modulating van der Waals attractions on a colloidal scale.

There is limited precedent for measuring and modeling van der Waals interactions between colloids and materials with spatially nonuniform and anisotropic dielectric functions, particularly when both effects occur simultaneously (as with interfacial PLC defects). For example, van der Waals interactions are understood to mediate interfacial LC orientations,[21-23] but liquid crystalline states allow orientational rearrangements as part of energy minimization. Van der Waals interactions between oriented anisotropic solid materials,[24-25] including birefringent solids,[26] are known from theoretical models to produce both forces and torques. However, direct force measurements between birefringent minerals have probed either oriented uniform single crystal mica[27-28] or average interactions between multiple oriented domains in a polycrystalline rutile titanium dioxide colloid with a single crystal of the same material.[29] Spatially nonuniform dielectric functions are theoretically known to mediate local van der Waals attraction,[30-33] which has been directly measured between surfaces with roughness,[34] adsorbed polymer,[35] and gold patterns.[16] Despite this precedent, prior studies have not directly modeled or measured van der Waals interactions between colloids and surfaces with dielectric functions that are spatially nonuniform, continuously varying, and anisotropic (as in interfacial PLC defects).

Here, we employ concentrated diffusing colloids to probe colloid-surface energy landscapes near topological defects at planar PLC surfaces. The conceptual development and practical demonstration of diffusing colloidal probes to measure *kT*-scale interfacial energy landscapes was originally shown for surface topography mediated gravitational energy landscapes.[36] In this prior case, surface topography could be independently and accurately characterized as part of validating the analysis. In this work, we employ diffusing colloidal probes using similar measurements and analyses with limited adaptation to obtain energy landscapes in the vicinity of PLC topological defects. However, for PLC surfaces: (1) surface topography may or may not contribute, (2) independent methods are not available to probe *kT*-scale energy landscapes,[37] and (3) theories to predict such landscapes have yet to be developed.

In the following, we describe the use of optical microscopy to measure the time-averaged spatial organization of colloids in dynamic equilibrium over PLC defects. PLC birefringence maps

at defects are independently characterized. Spatially varying particle density profiles analyzed with inverse Monte Carlo (MC) yield position-dependent particle-surface potential energy landscapes at PLC defects. The inverse MC analysis extends our prior approach to analyze diffusing colloids on physical topographical surface patterns,[36] where concentrated colloids diffuse more quickly over surfaces, sample higher energies, and provide a natural gauge of kT-scale energy landscapes. We have previously used evanescent wave scattering from dilute colloidal probes to map van der Waals landscapes,[16] but such an approach is not easily implemented with PLC optical properties. Sterically stabilized diffusing probes are employed to interrogate longer-range retarded van der interactions, which are both less sensitive to surface roughness and more sensitive to material dielectric functions (across a broad frequency range).[34] By using concentrated diffusing colloidal probes, the approach in this work is designed to overcome limitations with applying either single diffusing colloidal probes[16, 38] or mechanical scanning probes.[27-29] Ultimately, measured kT-scale energy landscapes are compared to spatially varying PLC optical properties around topological defects to quantitatively connect local interactions and interfacial properties. Understanding how spatially varying anisotropic dielectric profiles mediate local van der Waals attraction provides a basis to design surfaces to pattern colloidal microstructures and to mediate a range of other related interfacial phenomena.

Materials & Methods

Polymerized Liquid Crystal Materials. Chemicals were used as received from the manufacturers without additional purification. The nematic LC 4-cyano-4′-pentylbiphenyl (5CB, >99.5%) was obtained from Jiangsu Hecheng Advanced Materials Co., Ltd. (Nanjing, China). Reactive mesogen 1,4-bis[4-(3-acryloxyloxypropyloxy]-2-methylbenzene (RM257, >95%) was obtained from BOC Sciences (Shirley, NY). The photo-initiator, 2-dimethoxy-2-phenylacetophenone (DMPA, >99%), toluene (≥99.5%), dimethyloctadecyl[3-(trimethoxysilyl)propyl] ammonium chloride (DMOAP, 42 wt% in methanol), and glycerol (≥99.5%) were obtained from Sigma-Aldrich (St. Louis, MO). Fisherfinest premium grade glass slides were purchased from Fisher Scientific (Pittsburgh, PA). Copper transmission electron microscope grids (286 μm x 286 μm x 18 μm) were obtained from Electron Microscopy Sciences (Hatfield, PA). Purification of water (18.2 MΩ cm resistivity at 25 °C) was performed using a Milli-Q water system (Millipore, Bedford, MA, USA). Triethanolamine (TEA) HCl (99%) was purchased from Aldrich (Milwaukee, WI).

PLC Film Synthesis. All PLC films were synthesized from mixtures of 5CB, RM257, and DMPA placed into the pores of a 75 mesh copper TEM grid supported on a DMOAP-coated glass slide to promote perpendicular anchoring at the glass-LC surface. The LC mixture was prepared by vortexing 20 mg of RM257, 2 mg of DMPA, 80 μL of 5CB, and 40 μL of toluene (a cosolvent to facilitate mixing) in a glass vial. After the solids were dissolved, the vial was loosely covered with aluminum foil and left open to atmosphere overnight in a fume hood to evaporate off the toluene. Immersion of the supported LC-filled grid under a water-glycerol mixture (50/50 v/v) imparted planar surface anchoring at the LC-aqueous interface. Polymerization of the films was initiated by exposing the sample to long-wave ultraviolet light (365 nm, Spectroline E-Series Spectronics Corporation, Westbury, NY) for 10 minutes (2.5 mW/m² at a distance of 5 cm) at room temperature. Films were rinsed with water (20x of the volume of the 50/50 water/glycerol mixture) after polymerization before further analysis.

PLC Film Characterization. The orientation of the LC within the polymerized films was examined with optical microscopy (Olympus BX41) by using plane-polarized light in transmission mode with two rotating polarizers, 4x, 20x, and 50x objectives and a Moticam camera. A PolScope

(Polaviz, APSYS Inc., Chagrin Falls, OH) was used to measure the optical retardance of the LC films. The PolScope illuminates samples with circularly polarized light ($\lambda = 546.5$ nm) and images are collected with a Moticam camera. Optical profilometry of PLC films was performed using a Keyence VK-X260 laser-scanning profilometer (Itasca, IL) with a 50x long working distance objective after removal of the films from water and drying in air. Profilometry measurements were analyzed using VK-Viewer and VK-multifile software (Itasca, IL). Atomic force microscopy was performed using a Nanoscope IIIa atomic force microscope equipped with a fluid cell (Veeco Metrology Group, Santa Barbara, CA). Silicon nitride cantilevers with sharpened silicon nitride tips were used and measurements were performed in 10 mM aqueous TEA at pH 7.

Colloids and Polymer. Silica colloids of nominal 2.34 μm diameter (Bangs Laboratories) were rendered hydrophobic by coating with 1-octadecanol (Sigma-Aldrich) using a well-established literature method for creating highly stable dispersions.[39] Commercial PEO_{141}-PPO_{51}-PEO_{141} (F108 Pluronic) copolymer (M_w/M_n=1.2) was donated by BASF. To adsorb copolymer to colloids, 2 microliters of the hydrophobically modified 2.34 μm silica colloids was added to 500 microliters of the 1000ppm copolymer/deionized water solution and left to adsorb on a shaker overnight. The colloidal dispersion was washed several times with 1000ppm copolymer/deionized water before removing bulk copolymer via centrifugation. To adsorb copolymer to PLC interfaces, 1000 ppm PEO copolymer was dissolved in DI water and added to vacuum grease-sealed O-rings on the TEM grid/PLC film and left to equilibrate overnight under a coverslip. The bulk solution was then replaced with copolymer free deionized water several times via pipette. Prior to sedimentation of diffusing colloidal probes onto PLC patterns, copolymer coated silica colloids were processed via a repeated sedimentation fractionation process. After this step, 30 μL of these fractionated particles were placed in an O-ring that surrounded the supported TEM grid/PLC film and left to sediment around the LC defect of choice before recording particle trajectories.

Colloid Density Profiles on PLC Surfaces. Diffusing colloidal probes were tracked on PLC surfaces using a 63× objective (Zeiss LD Plan-NEOFLUAR, 0.75 numerical aperture objective) and a 12-bit CCD Camera (Hamamatsu Orca-ER) on an upright optical microscope (Axio Imager A1m, Zeiss). Images were recorded at 16 frames/s for 90 minutes to produce image stacks of ~89000 frames. 55x41 μm^2 images were obtained with 608 x 404 resolution to produce 100 nm pixels which allowed for centroid location using standard particle tracking algorithms. Density profiles were obtained by counting and averaging particle numbers in 2μm x 2μm bins.

Energy Landscapes from Inverse Monte Carlo. The following analysis is designed to extract the underlying potential energy landscape for single silica colloids interacting with PLC surfaces from microscopy measurements of non-uniform particle density profiles at equilibrium. The inverse MC analysis involves an algorithm to iteratively guess in a convergent process the position dependent particle-surface potential energy landscapes that matches simulated and measured particle density profiles (and inherently considers multi-particle packing, and entropy). This analysis is conceptually and practically similar to our previously reported algorithm,[36] which was specifically applied to analyze concentrated quasi-2D dispersions on gravitational potential energy landscape due to periodic surface topographies. The same analysis applies whether the surface is physically flat or not. Colloid density variation in the vicinity of PLC defects can be interpreted as an underlying colloid-surface potential energy landscape without assumptions about contributing interactions. Subsequent analysis of the potential energy landscape as the superposition of contributing potentials in described in the following theory section.

In brief, the inverse MC analysis involves a forward two-dimensional Monte Carlo (MC)

simulation in the canonical ensemble (NVT) implemented using the particle-particle potential in Eq. (11) and a position dependent particle-surface potential, $u_i(x,y)$. The particle-particle potential was first adjusted to match experimental two-dimensional radial distribution function as part of initializing the inverse MS algorithm. The inverse MC algorithm uses the forward MC simulation to obtain a density profile, $\rho_i(x,y)$, for a given potential energy, $u_i(x,y)$, which is compared to the experimental density profile, $\rho(x,y)$, and used to obtain a new potential as,[36]

$$u_{i+1}(x,y) = u_i(x,y) + 0.5kT\left[\frac{\rho_i(x,y)}{\rho(x,y)} - 1\right]$$ (1)

which is initialized with $u_{i=0}(x,y)=0$, particles evenly spaced on a hexagonal lattice, the particle number and simulation box size matched to experiments, and the density bins equated to image pixel dimensions. In each forward MC simulation, the equilibrium density profile, $\rho_i(x,y)$, was obtained during 10^5 steps following 10^6 equilibration steps. After the initial simulation, all subsequent simulations started with the final configuration from the previous iteration. Convergence was determined by minimization of the squared error within a threshold as,[36]

$$\chi_i = \sum_x \sum_y \left[\rho_i(x,y) - \rho(x,y)\right]^2$$ (2)

Theory

To interpret interfacial energy landscapes obtained from the inverse MC analysis, we specify a general theoretical model for spatially varying colloid-surface interactions based on the superposition of different contributions that could be position dependent based on local PLC properties (*i.e.*, LC anchoring orientation). In the context of measured results, we describe methods to adjust parameters within the following model to account for spatially varying energy landscapes. In the proposed models fit to experiments, all have net position dependent particle-surface interaction potentials, $u_{N,PS}$, for spherical colloids interacting with planar surfaces, at any given location, given by the superposition of van der Waals attraction, u_V, steric repulsion, u_S, and gravity, u_G, as,

$$u_{N,PS}(h) = u_V(h) + u_S(h) + u_G(h)$$ (3)

where h is particle surface-wall separation. The van der Waals sphere-surface interaction is,[40]

$$u_V(h) = \frac{a}{6}\int_h^\infty \frac{A(l)}{l^2}dl$$ (4)

where a is the sphere radius, and $A(l)$ is the separation-dependent interaction energy per area between half-spaces, which can be given by a form to capture retardation and screening as,[40]

$$A(l) = \frac{1}{2}[1 + 2\kappa l]\exp[-2\kappa l]A_0 + A_v(l)$$ (5)

where κ is the inverse Debye length, and A_0 and A_v (zero frequency and dispersion terms) can be computed by models of varying rigor.[41] This form accounts for the fact that the zero frequency term is screened by electrolyte but not retarded, and all higher frequency terms are not screened but are retarded. For a particle and surface of different materials "1" and "2" interacting across a medium of a material "3", an approximate expression for A_0 is given by,[42]

$$A_0 = \frac{3}{4} kT \left(\frac{\varepsilon_1 - \varepsilon_3}{\varepsilon_1 + \varepsilon_3} \right) \left(\frac{\varepsilon_2 - \varepsilon_3}{\varepsilon_2 + \varepsilon_3} \right) \tag{6}$$

where ε is each material's dielectric constant. An approximate expression for A_v is,

$$A_v = \frac{3h\nu}{8\sqrt{2}} \frac{\left(n_1^2 - n_3^2 \right) \left(n_2^2 - n_3^2 \right)}{\left(n_1^2 + n_3^2 \right)^{0.5} \left(n_2^2 + n_3^2 \right)^{0.5} \left[\left(n_1^2 + n_3^2 \right)^{0.5} + \left(n_2^2 + n_3^2 \right)^{0.5} \right]} \tag{7}$$

and n is each material refractive index, h is Planck's constant, ν is the primary dielectric adsorption frequency, k is Boltzmann's constant, and T is absolute temperature. A_0 and A_v can be computed rigorously using the Lifshitz theory,[41, 43] including the separation dependence of $A_v(l)$ due to retardation, but this requires more complete dielectric functions for all materials.[17, 26, 44] An approximate separation dependent $A_v(l)$ due to retardation, based on rigorous calculations for silica interacting across water[40] and silica interacting with polystyrene across water,[34] is given as,

$$A_v(l) = A_v (1 + 0.0143l) / (1 + 0.0593l + 0.0033l^2) \tag{8}$$

where A_v is the contact value (at $l=0$) from Eq. (7). The steric repulsion between adsorbed macromolecules for weak overlap can be modeled as,[45-46]

$$u_S(h, \Gamma) = \Gamma \exp(-\delta h) \tag{9}$$

where Γ and δ can be predicted[45, 47] or measured.[46, 48] The gravitational potential energy is,

$$u_G(h) = (4/3) \pi a^3 \left(\rho_p - \rho_f \right) gh = Gh \tag{10}$$

where ρ_p and ρ_f are particle and fluid densities, and g is acceleration due to gravity. As will be discussed in the context of analyzing measured energy landscapes, the gravitational potential energy can also be adjusted as a planar tilt to account for any locally flat surface not being perfectly level with respect to gravity.

Finally, the MC simulations require input of the particle pair potential, that is confirmed as part of the inverse analysis by matching experimental and simulated projected two-dimensional radial distribution functions. The net pair interaction potential, u_{PP}, between polymer coated colloids used in the simulations is,[45-46]

$$u_{N,PP}(r_{ij}) = u_S(r_{ij}) = (\Gamma/2) \exp\left[-\delta(r_{ij} - 2a) \right] \tag{11}$$

where r_{ij} is particle center-to-center separation.

The converged energy landscapes, $u_i(x,y)$, obtained from the inverse MC analysis are then modelled as the average in each bin of the particle-surface potential energy given in Eq. (3). The elevation averaged energy in each bin is,

$$\langle u(x,y) \rangle = \int_0^\infty u(x,y,h) p(x,y,h) dh \tag{12}$$

where $p(h)$ is the Boltzmann distribution given by,[49]

$$p(x,y,h) = p(x,y,h_m)\exp\left[\left(u(x,y,h) - u(x,y,h_m)\right)/kT\right] \qquad (13)$$

and $u(x,y,h)$ is particle-surface potential energy profile (Eq. (3)), and h_m is most probable height.

Results & Discussion

PLC Interfacial Defect Characterization

We first characterize optical and physical features on PLC surfaces in the vicinity of defects before proceeding to probe energy landscapes with diffusing colloidal probes (Fig. 1). **Fig. 1a** is a lower resolution optical image (crossed polars) of the PLC confined to a copper grid. The PLC film possesses escaped radial defects.[50] The defects themselves are located at the intersection of dark radial lines. **Fig. 1b** shows a higher resolution image (also crossed polars) of an isolated point
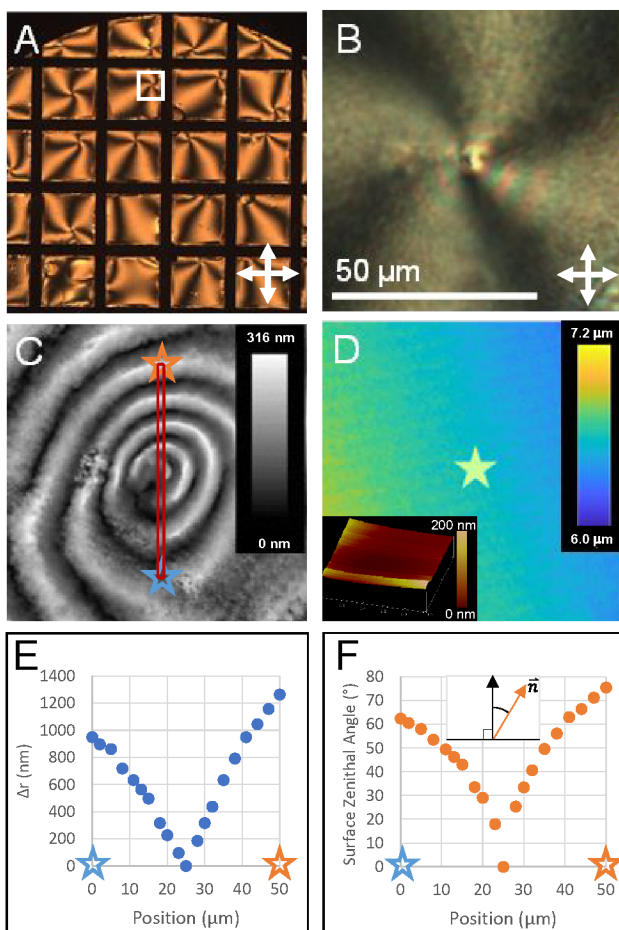
Fig. 1. Optical and topographical characterization of PLC interface. (A) A PLC sample in TEM grid (300 μm) imaged by cross-polarizers (double headed arrows show the orientation of the polarizer and analyzer). The white box (solid line) indicates the magnified region in panels B-D. **(B)** Magnified cross-polarization image of escaped radial point. **(C)** Optical retardance map of a PLC film for the same defect and lateral scale as in panel B. **(D)** Surface height profile of PLC film using (main) optical profilometry for the defect (star) and (inset) AFM in central 1μm x 1 μm region around similar defect (~20 nm z resolution). **(E)** Optical retardance, Δr, as measured along a trace in red rectangle in panel D including the surface defect, and **(F)** the calculated zenithal angle between LC director at the PLC surface, $\vec{n}$, and the surface normal. The uncertainty in the optical retardance and tilt angle values shown in E and F is smaller than the size of each symbol.

defect seen in **Fig. 1a**. Close inspection of this image reveals bands of interference colors (circular pink and green bands centered on the LC defect). Characterization of the defect in **Fig. 1b** with a PolScope retardance mapper (**Fig. 1c**) enables quantification of optical retardance vs. defect distance (**Fig. 1e**). By leveraging previously reported analyses,[51] optical retardance can be used to calculate spatial variations of the near-surface zenithal angle of the LC director, from the surface normal (**Fig. 1f**). Inspection of **Fig. 1f** reveals the near-surface LC orientation near the defect is parallel to the surface normal (or perpendicular to the interface), whereas, far from the defect, the near-surface LC orientation is orthogonal to the surface normal (or parallel to the interface). This finding is consistent with previous studies of escaped radial defects in PLC thin films.[50]

In addition to defect optical characterization, we characterized physical surface topography at the interfacial PLC defect. **Fig. 1d** shows a surface profile obtained using optical profilometry within a 50 μm x 50 μm square near the point defect (at the image center). The image shows no appreciable height variations within the profilometer resolution. The inset of **Fig. 1d** shows AFM characterization of the surface topography at much higher resolution within a 1 μm x 1 μm square region containing the defect. Again, no appreciable height variation in the immediate vicinity of the surface defect is discernable within the ~20 nm z-resolution of the AFM image. Taken together, the panels in **Fig. 1** demonstrate well-defined variations in optical properties within the defect region of PLC films that are topographically smooth.

Diffusing Colloidal Probes of PLC Interfaces

We next measure time-averaged equilibrium density profiles of colloidal particles free to diffuse over the PLC interface, which can be analyzed to probe interfacial properties that determine particle-surface interactions. As will be discussed in the following, variations in diffusing colloidal probe density profiles will be analyzed with inverse MC (see *Methods*) to reveal the underlying energy landscape, which we interpret as a superposition of colloid-surface potentials in Eq. (3). The particles have repulsive potentials via adsorbed polymer and do not aggregate, and the interaction of the particles with the substrate is on the order of the thermal energy *kT* so that irreversible deposition does not generally occur. As a result, particles dynamically sample equilibrium configurations within spatially non-uniform time-averaged density profiles that depend on the underlying position dependent potential energy landscape.

The experimental configuration consists of silica colloidal particles dispersed in water and sedimented onto the underlying PLC surface (**Fig. 2**). The hydrophobically modified colloids have an adsorbed PEG copolymer layer, and PEG copolymer is also adsorbed to the PLC surface. Although some electrostatic repulsion can be expected between the particle and PLC surface in low ionic strength aqueous media, the copolymer is required to generate repulsion between the colloids and surface so that no particles deposit and are free to sample lateral positions on the PLC. Electrostatic stabilization imparts kinetic stability via a finite energy barrier to deposition, whereas strong macromolecular repulsion produces thermodynamic stability via an essentially infinite barrier. The silica particles and PEG copolymer have been well characterized in prior studies including direct measurements of their interactions with a number of substrate surface in different conditions.[48, 52-54] We return to a quantitative analysis and discussion of the interactions after first describing results to quantify particle density profiles.

Fig. 2 shows an optical microscopy image of silica particles sedimented onto the PLC defect including particle tracking and a time averaged equilibrium density profile. **Fig. 2a** shows a raw unprocessed image of the silica particle probes, where a nearly central darker feature
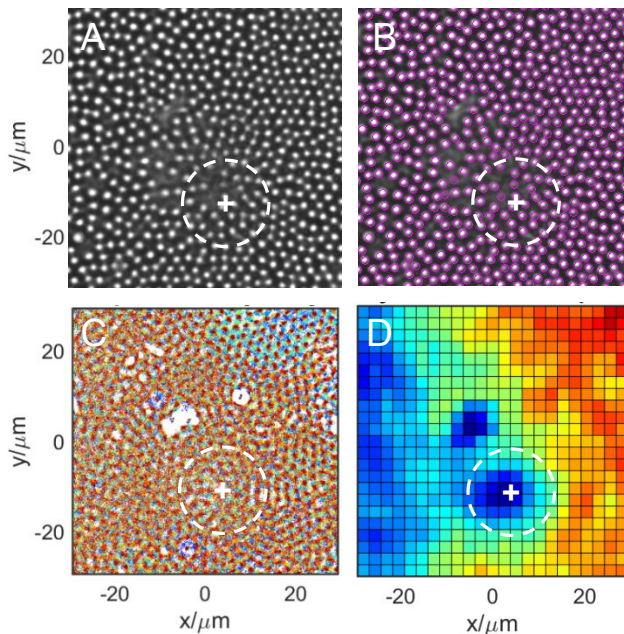
Fig. 2. Concentrated diffusing colloidal probes over PLC interface defect. Optical microscopy images (60um x 60um) of colloidal particles showing (**A**) raw, (**B**) center location, and (**C**) temporal trajectories (0-90 min (blue-red spectrum). (**D**) Time averaged density profile normalized by average density ($\rho(x,y)/<\rho>$ = 0.7-1.3, blue-red). From optical imaging in Fig. 1, the defect is located at $(x,y) = (5, -12)$ µm. To indicate the PLC defect location in each panel, a cross-hair approximates the defect center, and a 10 micron radius dashed circle approximates the optical retardance full width at half max (Figs. 1E,F).

indicates the PLC defect location. Image analysis (**Fig. 2b**) indicates successful tracking of each particle center coordinate using standard algorithms. Both images qualitatively show particle density profile variations near the defect and a more homogeneous distribution further away from the defect. **Fig. 2c** shows particle temporal trajectories indicating dynamic equilibrium behavior with no net drift. One or two deposited particles appear as white spots in Fig. 2c where other particles cannot access within one particle diameter.

By averaging the dynamic equilibrium trajectories from Fig. 2c for 90 min in 90,000 images, a time average density profile is obtained (**Fig. 2d**). The resulting density profile, $\rho(x, y)$, normalized by the average density, $\langle\rho\rangle$, shows a lower density in the vicinity of the defect as well as a density gradient across the observation window. The slight density variation across the image is consistent with a weak sedimentation equilibrium within the quasi-2D monolayer, which we discuss in subsequent analyses. The measured $\rho(x, y)$ and $\langle\rho\rangle$ were steady consistent with a dynamic equilibrium distribution. The bin size for constructing $\rho(x, y)$ is 2µm, which is similar to the particle probe diameter, and is also much greater than the particle-wall interaction region (via the Derjaguin approximation). The non-uniform equilibrium sampling by freely diffusing colloids of different surface locations is indicative of underlaying energy landscape, which we extract from analysis of the particle density profile in the following section.

PLC Interfacial Energy Landscape

In prior work, we analyzed concentrated quasi-2D dispersions to extract underlying energy landscapes – specifically for the case of a gravitational potential energy landscape due to periodic surface topographies.[36] As shown in **Fig. 1d**, the surface in this work is physically flat in the entire

observation window surrounding the PLC defect, but a colloid density variation in the vicinity of the defect suggests another contribution mediates the interactions of colloids with the underlying surface. A Boltzmann inversion of the measured density profile (*i.e.*, -ln[$\rho(x, y)$]) would yield a free energy landscape; the resulting free energy landscape would include contributions from both particle interactions with the underlying surface (potential energy landscapes) and particle packing effects (entropy landscapes) that together mediate lateral concentration profiles. In this work, we are interested in knowing the underlying potential energy landscape, which could in principle be mapped with dilute diffusing probes, as we have previously shown for mapping van der Waals landscapes from patterned gold films.[16] However, dilute particles are slow to statistically sample all surface locations and become localized within local potential energy wells $>5kT$. Concentrated particles more quickly diffuse over all surface locations with sufficient statistical sampling to map all positions. In addition, in concentrated dispersions, multi-particle packing effects cause particles to fill potential energy wells in such a way that particles more easily escape potential energy wells, and as a result, sample a greater range of energies.[36]

The goal in this work is to extract the underlying potential energy landscape from the measured particle density profiles, which we achieve using an inverse Monte Carlo scheme (see *Methods*). In brief, the approach broadly involves using an algorithm (Eq. (1)) to iteratively guess in a convergent process the energy landscape in the inverse MC scheme until the simulated and experimental density profiles agree within some tolerance (Eq. (2)). As a first step, the particle pair potential is specified (Eq. (11), **Table 1**), based on prior measurements[55] and checking agreement with the measured pair distribution function (see *Supporting Information*). Then, the relative potential energy of particles interacting with different positions is adjusted until experimental and simulated density profiles match.

Fig. 3 reports results for the converged equilibrated inverse MC simulation analysis. Results include a representative rendering of an equilibrated configuration (**Fig. 3a**), the simulated density profile (**Fig. 3b**) in agreement with experimental density profile (**Fig. 2d**), and the potential energy landscape for single silica colloids interacting with the PLC surface (**Fig. 3c**). The
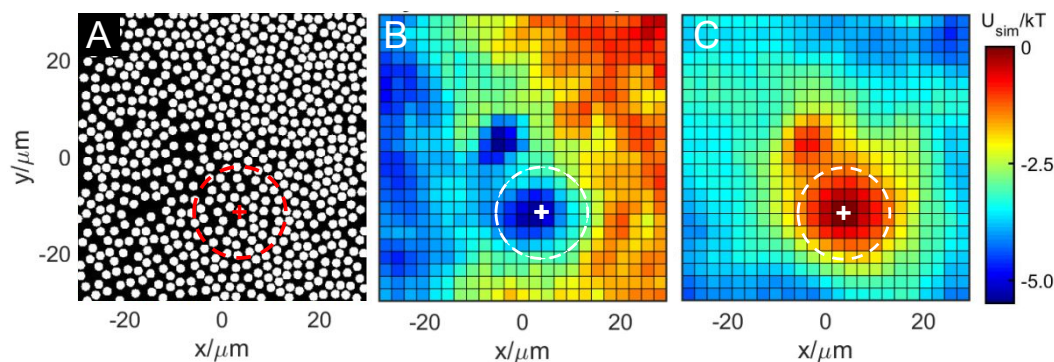
Fig. 3. Inverse MC simulation results for comparison to experimental results in Fig. 2. (**A**) Representative rendering of converged equilibrated inverse MC configuration. (**B**) Converged simulated density profile ($\rho(x,y)/<\rho>$ = 0.7-1.3, blue-red) for comparison with Fig. 2D. (**C**) Converged interfacial energy landscape determined from inverse MC simulation using Eq. (1). Panels A and B are reported prior to removing the effect of surface tilt, whereas panel C shows the net energy landscape after removing the effect of a surface tilt (~150 nm over ~50 μm) on the gravitational contribution. To indicate the PLC defect location in each panel, a cross-hair approximates the defect center, and a 10 micron radius dashed circle approximates the optical retardance full width at half max (Figs. 1E,F).

simulation matches the density variations in the experiments, including fewer particles at the PLC defect, and a shallow gradient from lower to higher density from the lower right to the upper left. As described in the *Methods*, the effect of any local tilt of the sample surface on the gravitational contribution to the particle density profile is effectively removed to yield the energy landscape due to colloid-surface interactions in **Fig 3c**. The shallow density gradient is harder to see in the single rendered configuration (**Fig. 3a**) but is more easily resolved from the accumulated statistics in the dynamically sampled time averaged density profile (**Fig. 3b**). The inverse MC simulation also captures a low-density aggregate at $(x,y)=(-4,2)$, which demonstrates the capability of the analysis to cope with realistic experimental issues. Since the aggregate is unrelated to probing the PLC interface defect, in the following we disregard further analysis of this feature.

The position-dependent energy landscape of individual colloidal probes interacting with the PLC surface indicates a potential energy maximum at the defect, $(x,y)=(3,-12)$, compared to the surrounding region (**Fig. 3c**). As expected, this local energy maximum occurs at the defect where the particle density is at a minimum. Because the effects of multi-particle packing, and entropy, are effectively considered as part of the inverse MC analysis, the observed energy maximum is due to the single particle-surface interaction at that position. The particle-surface energy is $\sim 4kT$ greater than the average particle-surface interaction far away from the defect. The energy decays from the local maximum over ~ 20 μm. Interestingly, the decay range in the particle-surface interaction energy is comparable to the range over which the LC surface orientation transitions from perpendicular to parallel for the escaped radial defects shown in **Fig. 1**.

We note here that we could have performed an inverse analysis based on three-dimensional forward MC simulations using particle-surface potentials, which would conceptually and numerically produce the same result as the approach we take here. The approach we instead take is to produce an intermediate two-dimensional energy landscape that we can interpret in a subsequent analysis step. Practically, since we don't measure elevation directly in experiments, we considered it appropriate to perform a two-dimensional inverse MC analysis of the measured two-dimensional density profiles that yields a two-dimensional energy landscape, which requires no assumptions (but can be analyzed for further interpretation). We have previously used evanescent wave scattering to directly measure three dimensional Brownian motion in dilute quasi-2D colloidal monolayers,[49, 56] but such an approach is not possible in concentrated monolayers due to multiple scattering, and generation of a well-defined evanescent wave at the PLC interface is non-trivial due to the spatially varying optical properties within the film.

In the following, we explore models of particle-surface potentials to understand the interactions that mediate the measured two-dimensional energy landscape in **Fig. 3c**. We then discuss these models in the context of the measured LC interfacial anchoring and director profile in the defect vicinity.

Overview of Interpreting PLC Interfacial Energy Landscapes

The energy landscape obtained from the inverse MC analysis is the average interaction of the diffusing particle probes with different lateral positions on the PLC interface. To interpret this measure of the interfacial energy landscape, we consider the energy at each position to be the average particle-surface potential energy normal to the interface. More precisely, for each bin in the two-dimensional energy landscape in **Fig. 3c**, we model the net particle-surface interaction potential as a superposition of contributing interactions (Eq. (3)), and then take the average of the elevation dependent energy (Eq. (12)). Because diffusing probes are sampling a three-dimensional

energy landscape, which is thin compared to the particle dimensions, we can "project" the three-dimensional landscape to a two dimensional landscape via Eq. (12).

In the following, we consider three models for the net particle-surface potential in each energy landscape location (Eq. (3)), each with a single adjustable parameter and all other parameters fixed (**Table 1**). As an initial step in all analyses, any mis-leveling of the sample cell or local slope of the PLC surface was accounted for by subtracting a gravitational planar tilt energy at every pixel. The planar tilt was obtained by a least squared error fit to the converged energy landscapes, $u_i(x,y)$, in the four corners away from the central defect region. Accounting for tilt was not an issue in our prior analysis of gravitational potential energy landscapes on topographically patterned surfaces,[36] so it is a novel aspect of modeling the energy landscape in this work. The optical table and microscope stage were both levelled with respect to gravity, but the observed PLC height variation of ~150 nm over a ~50μm lateral distance could easily arise due to changes in the polymerized surface within the grid or any non-planar variations in the grid itself.

Interpreting Energy Landscapes: Simplest Fit van der Waals Landscape (Model 1)

In our first attempt to model the energy landscape from inverse MC, we explore varying only the van der Waals contribution at each surface location according to estimates from available spectral data and a single adjustable parameter. In particular, the macromolecular repulsion is fixed to match previous direct measurements (**Table 1**),[46, 48] and the van der Waals attraction is specified using Eq. (4) with the $A_\perp$ values in **Table 1**, where the $A_\perp$ values correspond to liquid crystal properties associated with interfacial perpendicular orientation used in Eqs. (5)-(8). Spatial variations in the van der Waals attraction are then accounted for using an adjustable position dependent multiplier, $X(x,y) \times u_V$, in Eq. (3). We constrain $X(5\mu m, -12\mu m)=1$ at the PLC defect to consider the perpendicular LC orientation at that location. We then fit the energy landscape obtained from inverse MC in **Fig. 3c** to Eq. (3) (via Eq. (12)) by adjusting $X(x,y)$ at every position. Practically, the goal of this first fitting method is to investigate whether the van der Waals attraction can be fixed to an estimate based on the optical properties for perpendicular LC anchoring at the defect, and then see how much the van der Waals must vary at other positions relative to a fixed range of macromolecular repulsion.

Table 1. Parameters for potentials in Eq. (3) to analyze inverse MC energy landscapes. Values include: (a) steric repulsion pre-factor and decay length,[24, 26] (b) Debye length and particle size,[49] (c) and particle and medium material properties,[57] (d) liquid crystal characterization,[58-59] (e) Eqs. (5)-(8).

parameter (units)	value	parameter (units)	value
Γ^a (kT)	1984	ε (silica,[c] water,[c] LC$_{\parallel}$,[d] LC$_\perp$[d])	3, 78, 18.4, 6.8
δ^a (nm^{-1})	0.283	n (silica,[c] water,[c] LC$_{\parallel}$,[d] LC$_\perp$[d])	1.46, 1.6, 1.71, 1.53
κ^b (nm^{-1})	0.033	A(l=0)$_{\parallel}$, A(l=0)$_\perp$[e] (10^{-20}J)	1.12, 0.89
a^b (μm)	1.09	A$_{0,\parallel}$, A$_{0,\perp}$[e] (10^{-20}J)	0.21, 0.24
ρ(silica,[c] water[c]) (g/cm^3)	1.96, 1.00	A$_{v,\parallel}$, A$_{v,\perp}$[e] (10^{-20}J)	0.91, 0.65

The resulting van der Waals landscape (*i.e.*, $X(x,y) \times u_V$) evaluated at an elevation corresponding to the onset of macromolecular repulsion is shown in **Fig. 4a**, and the fitted coefficient $X(x,y)$ is shown in **Fig. 4d**. The onset of macromolecular repulsion occurs at the particle-surface separation when two adsorbed polymer brushes initially come into contact with $0.1kT$ energy (Eq. (9)), which is given by,

$$2L_0 = -\delta^{-1} \ln\left(0.1kT\Gamma^{-1}\right) \tag{14}$$

where L_0 is taken as the single uncompressed brush layer dimension. A cross section of the elevation dependent van der Waals landscape through the PLC defect center (x,h plane at $y=$-12μm) is shown in **Fig. 4g**. The dashed line in **Fig. 4g** indicates the onset of repulsion at $h=2L_0=34$nm. These results show how the van der Waals landscape depends on position in the lateral and normal directions relative to the PLC defect based on the equilibrium distribution of diffusing colloidal probes. The lateral radial dependence of the van der Waals landscape correlates spatially with the colloidal density (**Figs. 2, 3**) and PLC optical property variations (**Fig. 1**). In short, this model of radially varying van der Waals attraction based on LC interfacial anchoring is consistent with the colloid density variations in experiments and simulations and the LC optical properties.

This first model shows it is possible to adjust a spatially varying van der Waals contribution to capture the measured PLC energy landscape (**Fig. 3**). Furthermore, the van der Waals attraction when estimated based on the LC optical properties (Fig. 1) with perpendicular anchoring at the
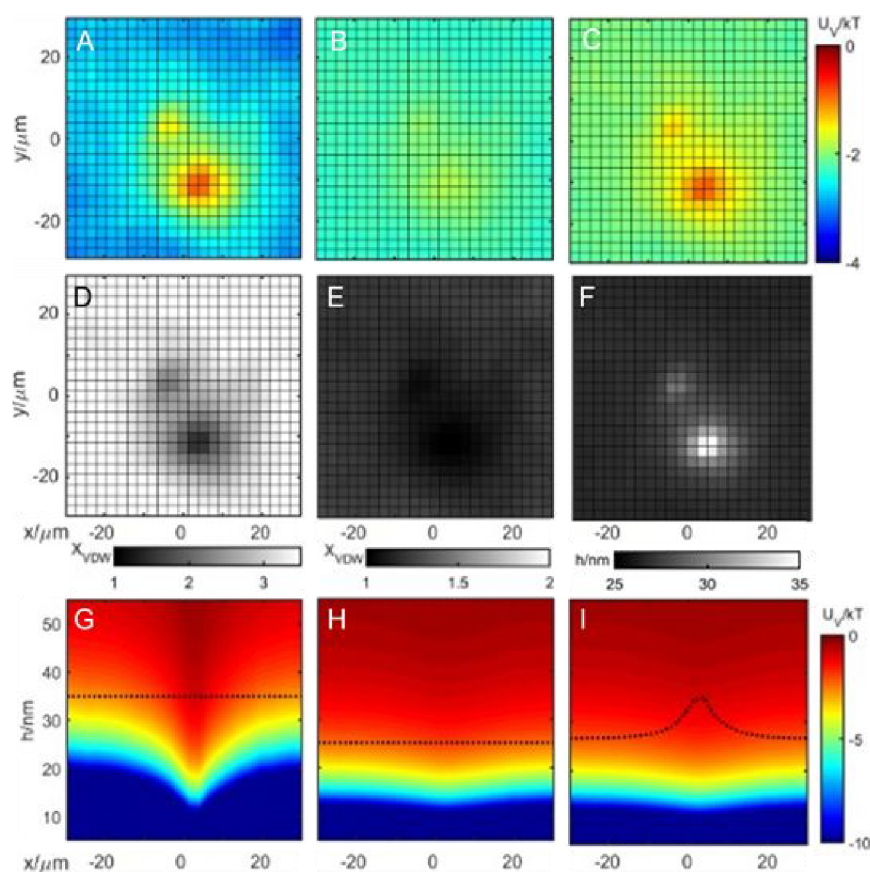
Fig. 4. Analysis of interfacial energy landscapes as superposition of contributing potentials. The following results show three models (see *Methods*) for superposition of van der Waals, steric, and gravitational potentials (Eq. (3)) for silica colloidal probes interacting with PLC interface with different adjustable parameters. For each model, rows show (top, **A-C**) van der Waals landscape is shown evaluated at the onset of macromolecular repulsion, $h=2L_0$ (Eq. (14)), (middle, **D-F**) the position dependent van der Waals multiplier, $X(x,y)$, in the first two models (see text for description), and the position dependent brush thickness, $(2L_0(x,y)$, in the last model, (bottom, **G-I**) Elevation dependent van der Waals landscape sliced through the defect center (at $y=$-8μm), and dashed line showing the brush layer thickness at $h=2L_0$ (Eq. (14)). Columns indicate: (left) model 1 (adjustable van der Waals pre-factor), (middle) model 2 (specified van der Waals pre-factor, adjusted uniform steric pre-factor), and (right) model 3 (specified van der Waals pre-factor, adjusted position dependent steric pre-factor).

defect can be adjusted within a factor of ~3 to account for all observed variations. However, the fitted factor of ~3 variation in the van der Waals attraction is greater than what seems possible based on the contact values of $A(l=0)_{\parallel}$, and $A(l=0)_{\perp}$ in **Table 1**, where their ratio is $A(l=0)_{\parallel}/A(l=0)_{\perp}=1.12/0.89=1.26$. Although the gravitational potential energy of the particles in this work is essentially certain via numerous prior measurements, and the macromolecular layer on the particles has also been repeatedly measured to the same value (e.g., refs[24, 26]), the copolymer layer on the PLC interface has not been previously characterized, which provides another interaction to consider in subsequent models.

Interpreting Energy Landscapes: Fixed van der Waals Landscape & Steric Adjustment (*Model 2*)

Because the first model shows the promise of quantifying the net colloid-PLC interfacial energy landscape by varying only the van der Waals contribution within a reasonable range of magnitudes, we next investigate a more rigorous model that more directly connects the van der Waals landscape to the PLC birefringent properties. In particular, the second model again specifies the position dependent van der Waals landscape as, $X(x,y)\times u_V$, but now with $X(x,y)=1+[(A(l=0)_{\parallel}/A(l=0)_{\perp})-1]u_i(x,y)$, where the $A_{\perp}$ and $A_{\parallel}$ values correspond to liquid crystal properties associated with interfacial perpendicular and parallel orientations (**Table 1**) used in Eqs. (5)-(8). The equation for $X(x,y)$ is based on a mixing rule determined by the local energy landscape value and the ratio $A(l=0)_{\parallel}/A(l=0)_{\perp}$ (inspired by prior work,[20] but with key differences captured in Eqs. (4)-(8)).

By fixing the van der Waals landscape to a model with no adjustable parameters, it is necessary to adjust another potential to optimize the fit the measured energy landscape. Now, the adjustable parameter in model 2 is the separation at which brushes contact, which is practically adjusted via Γ in the thickness in Eq. (14) and in the potential in Eq. (9). Because Γ is chosen as a constant in model 2, the average energy cannot be obtained exactly in each location (via Eq. (12)), but rather the least squared error is minimized over all position to determine the best Γ value. The goal of this second fitting method is to test whether the van der Waals landscape can be independently estimated based on the PLC optical properties, while also allowing for a different range of uniform macromolecular repulsion as an adjustable parameter.

For model 2, information on the resulting van der Waals landscape and range of macromolecular repulsion are reported in **Figs. 4b,e,h** with the same formatting as equivalent quantities for model 1 in Figs. **4a,d,g**. The results in **Fig. 4b** show the van der Waals landscape at polymer contact is much shallower than from model 1 (**Fig. 4a**), which is expected since the van der Waals is constrained to expected limits for planar and perpendicular anchoring based on the LC optical properties. The shallow van der Waals landscape is reflected in the constrained $X(x,y)$ that varies from 1-1.26 in **Fig. 4e**. Comparison of **Fig. 4h** and **Fig. 4g** on the same spatial and energy scales also captures how the entire van der Waals landscape is weaker, and particularly at the shorter contact distance of the adsorbed polymers layers, which occurs at $h= 2L_0=23$nm.

Model 2 has the desirable outcome that it captures the PLC defect energy landscape based on a reasonable model for the van der Waals based on LC orientation and optical properties. Practically, the LC orientation from characterization in **Fig. 1** and literature refractive indices and dielectric constants produce a van der Waals landscape based on well-established simple models for colloid-surface van der Waals attraction. It can also be noted that the range of van der Waals on the order of ~50nm in this work is also approximately dependent on material properties within the PLC film to a similar depth (see van der Waals film models[30, 41, 60]). As a result, it is reasonable

that surface anchoring at the LC interface is of sufficient depth to influence the van der Waals landscape measured in this work.

Allowing the adsorbed macromolecular repulsion to occur at a different separation in the model 2 fit is reasonable since the adsorbed polymer thickness has not previously been characterized on the PLC interface. The adsorbed copolymer thickness on the hydrophobic silica particles is well established in independent measurements to be L_0=17nm,[46, 48] and the thickness on hydrophobic spin coated polystyrene and signalized glass microscope slides also appears similar with L_0=17nm, including in asymmetric macromolecular interactions.[48, 53] The copolymer brush layer thickness on hydrophobic surfaces is considered to be a maximum due high adsorbed amounts and lateral chain crowding, and much thinner layers are known to form on hydrophilic surfaces.[61] The fitted onset of repulsion at h=23nm in model 2 suggests a copolymer layer thickness of L_0=6nm on the PLC interface. A thinner adsorbed copolymer layer on the PLC interface is reasonable based on known material properties and characterization.

Interpreting Energy Landscapes: van der Waals & Steric Landscapes (*Model 3*)

We explore a final model that fits Eq. (3) to the measured energy landscapes by considering our best available model for spatially varying van der Waals landscape (model 2), but now with the goal of achieving an exact fit at all surface locations by also allowing for position dependent polymer layer interactions. As we discuss in the following, allowing for position dependent polymer interactions can also be considered as a surrogate for any other unmodelled interactions, or collection of interactions, related to the PLC director profile. In more detail, the third model is fit to the inverse MC energy landscape by letting the polymer layer thickness on the PLC interface vary with position, which contrast the simpler assumption of a single layer dimension in model 2 (based on error minimization without an exact fit at all surface positions). In model 3, the van der Waals landscape is again specified based on interfacial optical properties as in model 2, but now the brush thickness and range of repulsion on the PLC interface is adjusted at each position via $\Gamma(x,y)$ in Eq. (14) and in the potential in Eq. (9). This model eliminates all errors between theory, simulation, and experiment by allowing additional adjustability at each PLC interface position. The goal of the third fitting method, similar to second model, is to investigate whether the van der Waals landscape can be independently estimated based on the PLC optical properties, but now also allow for non-uniform adsorbed polymer layers to capture the additional energy landscape variations at every position on the PLC interface relative to the defect.

The model 3 results are reported in **Figs. 4c,f,i**. **Figs. 4c,i** are reported in the same format as analogous plots in **Fig. 4** for models 1 and 2. Because the van der Waals landscape is determined in the same manner as model 2, instead of re-plotting the same result for $X(x,y)$ as in **Fig. 4e**, we instead plot in **Fig. 4f** the value of $2L_0(x,y)$ based on $\Gamma(x,y)$ in Eq. (14). The van der Waals landscape at contact in **Fig. 4c** again shows greater variations between the defect center and surrounding region, and the range of polymer repulsion is now greatest at the defect center in **Figs. 4f,i**. By attributing all local energy differences to variations in local macromolecular repulsion (after setting the van der Waals landscape), the combined layer dimensions vary from a maximum of $2L_0$=32nm at the defect center to $2L_0$=24nm away from the defect. If the polymer thickness is 17nm on the silica particle (based on prior work,[46, 48] then the polymer layer on the PLC would vary from 15nm on the defect to 7nm on the surrounding surface away from the defect.

Results from fitting model show the inverse MC energy landscape can be captured by a first principles van der Waals landscape, using known material properties, and a relatively minor

additional adjustment to the position dependent particle-surface interaction. In particular, modeling the van der Waals landscape based on PLC optical properties captures the net energy landscape, provided that an increased position dependent repulsion as included in the vicinity of the defect. We specifically model the increase repulsion at the defect as an increased polymer layer thickness, which would have to require a different local PLC material property to mediate such an increasing layer dimension at the defect. As already noted, hydrophobicity mediates copolymer adsorbed amounts[61] and lateral interactions determining chain extension and brush architecture.[62] However, the apparent slight increase in repulsion at the defect could also be accounted for in the net potential via locally weaker van der Waals, increased electrostatic repulsion, increased polymer repulsion, or combinations of changes in all three potentials

Because limited information is available for PLC interfacial properties as a function of LC orientation, particularly around defects, it is not obvious what other properties and resulting colloid-surface interactions may be influenced by local interfacial LC orientation. We have not considered electrostatic interactions thus far in the analysis, primarily because adsorbed nonionic polymer on the particle and wall are known to significantly reduce the surface electric potential.[63] In preliminary studies of the same silica colloids on the PLC interface in the absence of polymer in deionized water, electrostatic stabilization was marginal (compared to the same particles on glass[36, 56] or gold[16]); this indicated the native surface charge density and electric potential are relatively low to start with, and the motivated the use of adsorbed polymer stabilization. Adsorbing polymer will further reduce the surface potential. Nevertheless, electrostatics could still contribute a finite repulsive interaction, that could also be position dependent based on LC interfacial orientation and any local electrostatic effects. In short, other small changes in kT-scale interactions due to local LC orientation could also contribute to the spatially varying energy landscape in this work, but the results in **Fig. 4** suggest it can primarily be captured by superposition of a position dependent van der Waals contribution and macromolecular repulsion.

Generality to PLC Defects

To demonstrate the generality of the findings in **Figs. 1-4**, we performed a number of similar measurements with quantitatively similar results. We show additional representative examples in **Fig. 5** and worked up in full detail in **Figs. S1-S3** based on model 3. Each sample is from independent experiments on different preparations of PLCs in TEM grids. Optical characterization includes cross-polarizer and retardance map images for each defect, and physical characterization shows each defect to be topographically smooth. The birefringence maps for each defect reflect differences throughout the entire PLC film where thicker samples include more concentric rings. However, in each case, the polarization and birefringence images correspond to the expected interfacial LC radial director profile transitioning from perpendicular to parallel anchoring around the escaped radial defect. The interfacial LC profiles are also expected to be of sufficient depth to determine the van der Waals landscape for the range of interactions normal to the interface (~50nm interaction range, approximately depends on material properties within the PLC film to a similar depth, see van der Waals film models[30, 41, 60]).

In comparing the three measurements in **Fig. 5**, it should be noted that even before attempting to further interpret the raw two-dimensional energy landscapes from inverse Monte Carlo, they all exhibit a local energy maximum at the PLC defect center. Furthermore, the position dependence of the raw two-dimensional energy landscape correlates well with the measured spatial variations in PLC optical properties, which can also be directly connected to the spatially varying director profiles.[50] As a simple and clear result, the "raw" optical map and energy landscape data
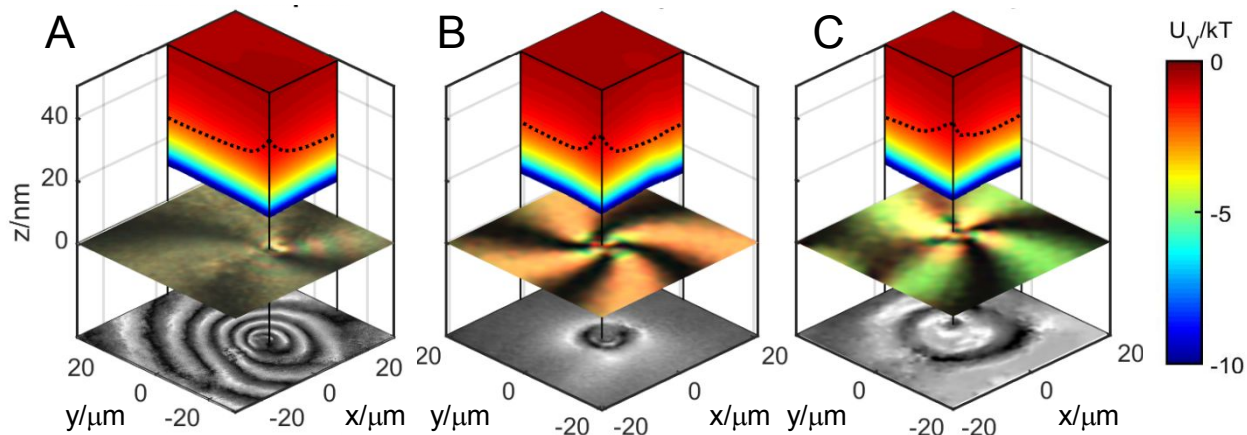
Fig. 5. Analyzed energy landscapes for silica colloids interacting with three different PLC defects. The energy landscapes are obtained based on model three (see *Methods*, right column Fig. 4). Each result shows optical characterization images and an energy landscape (Eq. (3)) quadrant cross sectional view centered on the defect with a dashed line showing the brush layer thickness at $h=2L_0$ (Eq. (14)). For each case, complete results are reported in *Supporting Information* including microscopy images, simulation renderings, density profiles, and fitted data similar to the plots in Fig. 4.

are correlated without any further interpretation. Modeling the energy landscapes as the superposition of van der Waals and repulsive interactions also produces van der Waals landscapes with spatial variations that strongly correlate with the PLC optical property variations (without assumptions that impose such a correlation). As in **Fig. 4**, quantitative modeling of the measured net energy landscape again requires an enhanced repulsion in each case in **Fig. 5**, but this may be partly due to limitations of the van der Waals model. Overall, these data support the general conclusion that an anisotropic dielectric function linked to the PLC director profile mediates the van der Waals contribution in the measured energy landscapes.

　　　　Finally, we discuss here in more detail the limitations of our simple van der Waals model (Eqs. (4)-(8)) and the opportunity for more rigorous calculations that might also account for small quantitative differences in the analyzed energy landscapes (**Figs. 4, 5**). For longer-range van der Waals contributing beyond the range of macromolecular repulsion, the interaction is screened, retarded, and determined by the material dielectric functions over a broad frequency range (e.g., see ref. [34]). While we included screening of zero frequency contributions (Eq. (5)), and approximated retardation in terms of weakening long range interactions (Eq. (8)), the limited availability of spectral data at other frequencies can more significantly affect predictions of longer range retarded interactions.[17] Specifically, infrared and microwave frequency contributions have proportionally stronger contributions at larger separations where retardation is important.[34] In addition, although models exist for retarded van der Waals interactions between materials with anisotropic dielectric functions,[25] these are limited to oriented single domain materials and are not easily translatable to spatially varying anisotropic material properties as in PLC films. Shorter-range non-retarded van der Waals attraction relevant to irreversible colloidal deposition[20] and measurable by mechanical methods[27-29] is likely to be less sensitive to many of the above cited effects; however, *kT*-scale van der Waals attraction probed by diffusing colloids[16, 34] and important to colloidal assembly can depend significantly on screening, retardation, and accurate dielectric spectra. Despite known limitations of the relatively simple van der Waals model in this work, it captures the majority of the retarded van der Waals energy landscape based on analyzing the

equilibrium interaction of concentrated colloids with PLC defects.

Conclusions

Optical microscopy was used to measure the time averaged density profiles of diffusing colloidal probes on planar PLC surfaces near LC defects. Results reveal particle concentration profiles that are highly correlated with independently characterized spatially varying optical properties around LC defects. An inverse MC simulation method is used to extract two-dimensional kT-scale potential energy landscapes that indicate how colloid-surface interactions change as a function of position relative to PLC defects. These two-dimensional energy landscapes are also highly correlated with spatially varying PLC defect optical properties.

The energy landscapes are modeled as the superposition of macromolecular repulsion and van der Waals interactions based on an anisotropic dielectric function determined from LC birefringence. The resulting van der Waals landscape captures the majority of the net energy landscape variations and appears to be well correlated with estimates of spatially varying LC director profiles. The measured energy landscape near the defect center may require consideration of additional effects such as local changes in repulsive potentials or more rigorous retarded van der Waals models with complete spectral data and spatially varying anisotropic material properties. Our results also suggest the possibility of spatial variations of adsorbed polymer architectures and interactions on PLC interfaces, which is also perhaps worthy of further investigation.

Our findings indicate an approach to sensitively measure kT-scale van der Waals energy landscapes at PLC interfacial defects, which confirms their existence and connection to PLC optical properties. Given the measured van der Waals attraction vary by several kT, based on PLC anchoring orientation, these spatially varying interactions are precisely of a magnitude critical to influencing Brownian motion, diffusion, interfacial phase behavior, and equilibrium self-assembly processes. Understanding the origin of van der Waals landscapes can enable the design and fabrication of interfacial energy landscapes from LCs, birefringent minerals, and 2D van der Waals heterostructures, which could be used for interfacial colloidal assembly of particle-based materials.

Acknowledgments

Supporting Information

Electronic supplementary information is available, including additional microscopy images, simulation renderings, density profiles, and energy landscapes for different PLC defects.

References

1. Smoukov, S. K.; Gangwal, S.; Marquez, M.; Velev, O. D. Reconfigurable Responsive Structures Assembled from Magnetic Janus Particles. *Soft Matter* **2009,** *5*, 1285-1292.
2. McDougal, A.; Miller, B.; Singh, M.; Kolle, M. Biological Growth and Synthetic Fabrication of Structurally Colored Materials. *Journal of Optics* **2019,** *21*, 073001.
3. van Blaaderen, A.; Ruel, R.; Wiltzius, P. Template-Directed Colloidal Crystallization. *Nature* **1997,** *385*, 321-324.
4. Yin, Y.; Lu, Y.; Gates, B.; Xia, Y. Template-Assisted Self-Assembly; a Practical Route to Complex Aggregates of Monodispersed Colloids with Well-Defined Sizes, Shapes, and

Structures. *J. Am. Chem. Soc.* **2001,** *123*, 8718-8729.

5.   Kraus, T.; Malaquin, L.; Schmid, H.; Riess, W.; Spencer, N. D.; Wolf, H. Nanoparticle Printing with Single-Particle Resolution. *Nature Nanotechnology* **2007,** *2*, 570-576.

6.   Aizenberg, J.; Braun, P. V.; Wiltzius, P. Patterned Colloidal Deposition Controlled by Electrostatic and Capillary Forces. *Phys. Rev. Lett.* **2000,** *84*, 2997-3000.

7.   Fustin, C.-A.; Glasser, G.; Spiess, H. W.; Jonas, U. Parameters Influencing the Templated Growth of Colloidal Crystals on Chemically Patterned Surfaces. *Langmuir* **2004,** *20*, 9114-9123.

8.   Helseth, L. E.; Wen, H. Z.; Hansen, R. W.; Johansen, T. H.; Heinig, P.; Fischer, T. M. Assembling and Manipulating Two-Dimensional Colloidal Crystals with Movable Nanomagnets. *Langmuir* **2004,** *20*, 7323-7332.

9.   Hayward, R. C.; Saville, D. A.; Aksay, I. A. Electrophoretic Assembly of Colloidal Crystals with Optically Tunable Micropatterns. *Nature* **2000,** *404*, 56-59.

10. Kim, Y.; Shah, A. A.; Solomon, M. J. Spatially and Temporally Reconfigurable Assembly of Colloidal Crystals. *Nat. Commun.* **2014,** *5*, 4676.

11. Zhang, J.; Zhang, Y.; Bevan, M. A. Spatially Varying Colloidal Phase Behavior on Multi-Dimensional Energy Landscapes. *J. Chem. Phys.* **2020,** *152*, 054905.

12. Zhang, J.; Yan, J.; Granick, S. Directed Self-Assembly Pathways of Active Colloidal Clusters. *Angewandte Chemie International Edition* **2016,** *55*, 5166-5169.

13. Fernandes, G. E.; Beltran-Villegas, D. J.; Bevan, M. A. Spatially Controlled Reversible Colloidal Self-Assembly. *J. Chem. Phys.* **2009,** *131*, 134705.

14. Edwards, T. D.; Yang, Y.; Everett, W. N.; Bevan, M. A. Reconfigurable Multi-Scale Colloidal Assembly on Excluded Volume Patterns. *Sci. Rep.* **2015,** *5*, 13612.

15. Vossen, D. L. J.; Plaisier, M. A.; Blaaderen, A. v. *Colloidal Crystallization Induced by Optical Gradient Forces Exerted by Optical Tweezers*. SPIE: **2004**; Vol. 5514, p 755-762.

16. Wu, H.-J.; Everett, W. N.; Anekal, S. G.; Bevan, M. A. Mapping Patterned Potential Energy Landscapes with Diffusing Colloidal Probes. *Langmuir* **2006,** *22*, 6826-6836.

17. Moazzami Gudarzi, M.; Aboutalebi, S. H. Self-Consistent Dielectric Functions of Materials: Toward Accurate Computation of Casimir–Van Der Waals Forces. *Science Advances* **2021,** *7*, eabg2272.

18. Soyka, F.; Zvyagolskaya, O.; Hertlein, C.; Helden, L.; Bechinger, C. Critical Casimir Forces in Colloidal Suspensions on Chemically Patterned Surfaces. *Phys. Rev. Lett.* **2008,** *101*, 208301.

19. Smith, B. D.; Fichthorn, K. A.; Kirby, D. J.; Quimby, L. M.; Triplett, D. A.; González, P.; Hernández, D.; Keating, C. D. Asymmetric Van Der Waals Forces Drive Orientation of Compositionally Anisotropic Nanocylinders within Smectic Arrays: Experiment and Simulation. *ACS Nano* **2014,** *8*, 657-670.

20. Fuster, H. A.; Wang, X.; Wang, X.; Bukusoglu, E.; Spagnolie, S. E.; Abbott, N. L. Programming Van Der Waals Interactions with Complex Symmetries into Microparticles Using Liquid Crystallinity. *Science Advances* **2020,** *6*, eabb1327.

21. Smith, E. R.; Ninham, B. W. Response of Nematic Liquid Crystals to Van Der Waals Forces. *Physica* **1973,** *66*, 111-130.

22. Dubois-Violette, E.; De Gennes, P. G. Effects of Long Range Van Der Waals Forces on the Anchoring of a Nematic Fluid at an Interface. *Journal of Colloid and Interface Science* **1976,** *57*, 403-410.

23. Mushenheim, P. C.; Abbott, N. L. Hierarchical Organization in Liquid Crystal-in-Liquid

Crystal Emulsions. *Soft Matter* **2014,** *10*, 8627-8634.

24. Parsegian, V. A.; Weiss, G. H. Dielectric Anisotropy and the Van Der Waals Interaction between Bulk Media. *The Journal of Adhesion* **1972,** *3*, 259-267.

25. Dagastine, R. R.; Prieve, D. C.; White, L. R. Calculations of Van Der Waals Forces in 2-Dimensionally Anisotropic Materials and Its Application to Carbon Black. *J. Colloid Interface Sci.* **2002,** *249*, 78-83.

26. Bergstrom, L. Hamaker Constants of Inorganic Materials. *Advances in Colloid and Interface Science* **1997,** *70*, 125-169.

27. Tabor, D.; Winterton, R. H. S. The Direct Measurement of Normal and Retarded Van Der Waals Forces. *Proceedings of the Royal Society of London. A. Mathematical and Physical Sciences* **1969,** *312*, 435-450.

28. Israelachvili, J. N.; Tabor, F. R. S. D. The Measurement of Van Der Waals Dispersion Forces in the Range 1.5 to 130 Nm. *Proc. R. Soc. Lond. A.* **1972,** *331*, 19-38.

29. Larson, I.; Drummond, C. J.; Chan, D. Y. C.; Grieser, F. Direct Force Measurements between Titanium Dioxide Surfaces. *Journal of the American Chemical Society* **1993,** *115*, 11885-11890.

30. Weiss, G. H.; Kiefer, J. E.; Parsegian, V. A. Effects of Dielectric Inhomogeneity on the Magnitude of Van Der Waals Interactions. *Journal of Colloid and Interface Science* **1973,** *45*, 615-625.

31. Kiefer, J. E.; Parsegian, V. A.; Weiss, G. H. Model for Van Der Waals Attraction between Spherical Particles with Nonuniform Adsorbed Polymer. *J. Colloid Interface Sci.* **1975,** *51*, 543-546.

32. Dagastine, R. R.; Bevan, M. A.; White, L. R.; Prieve, D. C. Calculation of Van Der Waals Forces with Diffuse Coatings: Applications to Roughness and Adsorbed Polymers. *J. Adhesion* **2004,** *80*, 365-394.

33. Cole, M. W.; Velegol, D.; Kim, H.-Y.; Lucas, A. A. Nanoscale Van Der Waals Interactions. *Molecular Simulation* **2009,** *35*, 849-866.

34. Bevan, M. A.; Prieve, D. C. Direct Measurement of Retarded Van Der Waals Attraction. *Langmuir* **1999,** *15*, 7925-7936.

35. Bevan, M. A.; Prieve, D. C. Forces and Hydrodynamic Interactions between Polystyrene Surfaces with Adsorbed Peo-Ppo-Peo. *Langmuir* **2000,** *16*, 9274-9281.

36. Bahukudumbi, P.; Bevan, M. A. Imaging Energy Landscapes Using Concentrated Diffusing Colloidal Probes. *J. Chem. Phys.* **2007,** *126*, 244702.

37. Bevan, M. A.; Eichmann, S. L. Optical Microscopy Measurements of Kt-Scale Colloidal Interactions. *Curr. Opin. Colloid Interface Sci.* **2011,** *16*, 149-157.

38. Prieve, D. C. Measurement of Colloidal Forces with Tirm. *Adv. Colloid Interface Sci.* **1999,** *82*, 93-125.

39. van Helden, A. K.; Jansen, J. W.; Vrij, A. Preparation and Characterization of Spherical Monodisperse Silica Dispersions in Non-Aqueous Solvents. *J. Coll. Interfac. Sci.* **1981,** *81*, 354-368.

40. Bitter, J. L.; Duncan, G. A.; Beltran-Villegas, D. J.; Fairbrother, D. H.; Bevan, M. A. Anomalous Silica Colloid Stability and Gel Layer Mediated Interactions. *Langmuir* **2013,** *29*, 8835-8844.

41. Prieve, D. C.; Russel, W. B. Simplified Predictions of Hamaker Constants from Lifshitz Theory. *J. Coll. Interfac. Sci.* **1988,** *125*, 1.

42. Israelachvili, J. N. *Intermolecular and Surface Forces* 2nd ed.; Academic Press: San Diego,

1991.

43. Dzyaloshinskii, I. E.; Lifshitz, E. M.; Pitaevskii, L. P. The General Theory of Van Der Waals Forces. *Adv. Phys.* **1961**, *10*, 165-209.

44. Hough, D. B.; White, L. R. The Calculation of Hamaker Constants from Lifshitz Theory with Applications to Wetting Phenomena. *Adv. Colloid Interface Sci.* **1980**, *14*, 3-41.

45. Eichmann, S. L.; Meric, G.; Swavola, J. C.; Bevan, M. A. Diffusing Colloidal Probes of Protein–Carbohydrate Interactions. *Langmuir* **2013**, *29*, 2299-2310.

46. Jumai'an, E.; Garcia, E.; Herrera-Alonso, M.; Bevan, M. A. Specific Ion Effects on Adsorbed Zwitterionic Copolymers. *Macromolecules* **2020**, *53*, 9769-9778.

47. Milner, S. T. Compressing Polymer Brushes - a Quantitative Comparison of Theory and Experiment. *Europhysics Letters* **1988**, *7*, 695-699.

48. Petroff, M. G.; Garcia, E. A.; Dengler, R. A.; Herrera-Alonso, M.; Bevan, M. A. Kt-Scale Interactions and Stability of Colloids with Adsorbed Zwitterionic and Ethylene Oxide Copolymers. *Macromolecules* **2018**, *51*, 9156-9164.

49. Wu, H.-J.; Pangburn, T. O.; Beckham, R. E.; Bevan, M. A. Measurement and Interpretation of Particle−Particle and Particle−Wall Interactions in Levitated Colloidal Ensembles. *Langmuir* **2005**, *21*, 9879-9888.

50. Miller, D. S.; Carlton, R. J.; Mushenheim, P. C.; Abbott, N. L. Introduction to Optical Methods for Characterizing Liquid Crystals at Interfaces. *Langmuir* **2013**, *29*, 3154-3169.

51. Brake, J. M.; Mezera, A. D.; Abbott, N. L. Active Control of the Anchoring of 4'-Pentyl-4-Cyanobiphenyl (5cb) at an Aqueous−Liquid Crystal Interface by Using a Redox-Active Ferrocenyl Surfactant. *Langmuir* **2003**, *19*, 8629-8637.

52. Fernandes, G. E.; Bevan, M. A. Equivalent Temperature and Specific Ion Effects in Macromolecule Coated Colloid Interactions. *Langmuir* **2007**, *23*, 1500-1506.

53. Everett, W. N.; Wu, H.-J.; Anekal, S. G.; Sue, H.-J.; Bevan, M. A. Diffusing Colloidal Probes of Protein and Synthetic Macromolecule Interactions. *Biophys. J.* **2007**, *92*, 1005-1013.

54. Beltran-Villegas, D. J.; Edwards, T. D.; Bevan, M. A. Self-Consistent Colloidal Energy and Diffusivity Landscapes in Macromolecular Solutions. *Langmuir* **2013**, *29*, 12337-12341.

55. Edwards, T. D.; Bevan, M. A. Polymer Mediated Depletion Attraction and Interfacial Colloidal Phase Behavior. *Macromolecules* **2012**, *45*, 585-594.

56. Wu, H.-J.; Bevan, M. A. Direct Measurement of Single and Ensemble Average Particle-Surface Potential Energy Profiles. *Langmuir* **2005**, *21*, 1244-1254.

57. Lide, D. R. *Crc Handbook of Chemistry and Physics*. CRC Press: New York, **2000**; Vol. 80.

58. Horn, R. G. Refractive Indices and Order Parameters of Two Liquid Crystals. *J. Phys. France* **1978**, *39*, 105-109.

59. Ratna, B. R.; Shashidhar, R. Dielectric Studies on Liquid Crystals of Strong Positive Dielectric Anisotropy. *Molecular Crystals and Liquid Crystals* **1977**, *42*, 113-125.

60. Vold, M. J. The Effect of Adsoprtion on the Van Der Waals Interaction of Spherical Colloidal Particles. *Journal of Colloid Science* **1961**, *16*, 1-12.

61. Nejadnik, M. R.; Olsson, A. L. J.; Sharma, P. K.; van der Mei, H. C.; Norde, W.; Busscher, H. J. Adsorption of Pluronic F-127 on Surfaces with Different Hydrophobicities Probed by Quartz Crystal Microbalance with Dissipation. *Langmuir* **2009**, *25*, 6245-6249.

62. Fleer, G. J.; Stuart, M. A. C.; Scheutjens, J. M. H. M.; Cosgrove, T.; Vincent, B. *Polymers at Interfaces*. Chapman & Hall: New York, **1993**.

63. Barany, S. Polymer Adsorption and Electrokinetic Potential of Dispersed Particles in Weak and Strong Electric Fields. *Advances in Colloid and Interface Science* **2015**, *222*, 58-69.